2

Secondary Acidification

Mizuo Kajino[1] and Hiromasa Ueda[2]
[1]*Meteorological Research Institute, Japan Meteorological Agency,*
[2]*Toyohashi Institute of Technology,*
Japan

1. Introduction

Secondary acidification (Kajino et al., 2008), also referred to as indirect acidification (Kajino et al., 2005; Kajino & Ueda, 2007), is a process that involves accelerated acid deposition associated with changes in gas–aerosol partitioning of semivolatile aerosol components, such as nitric acid (HNO_3), hydrochloric acid (HCl), and ammonia (NH_3), even though emissions of these substances and their precursors (e.g., NO_x) remain unchanged. HNO_3, HCl, and NH_3 are thermodynamically partitioned into gas and aerosol (particulate) phases in the atmosphere. This partitioning depends on temperature, humidity, and the presence of other components such as sulfuric acid (H_2SO_4) and crustal cations (Na^+, Mg^{2+}, Ca^{2+}, and K^+). Among acidic components in the air, H_2SO_4 has an equilibrium vapor pressure very much lower than that of other acids. When H_2SO_4 concentrations increase, NO_3^- and Cl^- in the aerosol phase shift to the gas phase, which causes the concentrations (fractions) of gaseous HNO_3 and HCl to increase, although total nitrate (t-NO_3 = HNO_3 + NO_3^-) and total chloride (t-Cl = HCl + Cl^-) remain unchanged. The deposition velocities of the highly reactive gaseous phases of HNO_3 and HCl are larger than those of their aerosol phases. For example, measured dry deposition velocities of HNO_3 gas are 20 times those of NO_3^- aerosols (Brook et al., 1997). Moreover, HNO_3 and HCl gases both readily dissolve into cloud and rain droplets. For solution equilibrium, their Henry's law constants are 2.1×10^5 and 727 mol L^{-1} atm^{-1}, respectively, which are extremely large values compared with those of SO_2 and NO_2 (1.23 and 0.01 mol L^{-1} atm^{-1}, respectively). Thus, below-cloud scavenging coefficients of irreversibly scavenged gases such as HNO_3 and HCl are several times those of their corresponding aerosols (Jylhä, 1999a, 1999b). In-cloud scavenging processes of gases and aerosols are hard to compare by this simple estimation procedure, because in-cloud scavenging of aerosol phases involves complexity of cloud dynamical and microphysical processes. Model calculations supported by observational data are necessary to estimate which phases are more efficiently scavenged for determination of net (in-cloud and below-cloud) wet deposition.

The secondary acidification effect was first identified in volcanic SO_2 plumes (Satsumabayashi et al., 2004). Miyakejima volcano, 180 km south of Tokyo, has erupted continuously since July 2000, resulting in considerable SO_2 emissions into the troposphere. One year after the start of emissions measurement in September 2000 (Kazahaya, 2001), SO_2 emissions totaled 9 Tg, equivalent to half the 20 Tg of anthropogenic SO_2 emissions from China in 2000. According to ground-based observations of gases and aerosols at Happo Ridge observatory (1,850 m ASL, 300 km north of Miyakejima volcano), the fraction of gaseous HNO_3 and HCl in the Miyakejima volcanic plume exceeded 95% (September 2000),

whereas in the same season the fraction of these gases in contaminated air masses of the Asian continental outflow was approximately 40% (September, 1999). Consequently, the bimonthly mean NO_3^- and Cl^- concentrations in precipitation (net wet deposition) in August and September 2000 at Happo Ridge, after the eruption, increased by 2.7 and 1.9 times, respectively, compared with the same months in 1999, before the eruption.

Extensive studies of the seasonal and diurnal variations in gas–aerosol partitioning of semivolatile components and the mechanisms causing partitioning changes have been conducted (Moya et al., 2001; Lee et al., 2006; Morino et al., 2006). It was confirmed that the partitioning importantly influences surface fluxes of pollutants (Nemitz and Sutton, 2004) and climate (Adams et al., 2001; Schaap et al., 2004). The current study series on secondary acidification provides new evidence that changes in the gas–aerosol partitioning have important environmental impacts.

In section 2, we describe the secondary acidification process in detail. We present the results of our previous study series on secondary acidification due to the Miyakejima volcanic eruption in section 3, based on observational evidence (sect. 3.1) and modeling (sect. 3.2). In section 4, we describe secondary acidification occurring during long-range transport of anthropogenic air pollutants. We conduct an observational analysis (sect. 4.1) to reveal the current status, and perform model studies (sect. 4.2) to analyze possible future scenarios. We summarize our major findings in section 5. Here, we focus mainly on accelerated deposition of nitrate rather than that of chloride, because anthropogenic chloride emissions contain large uncertainty.

2. Secondary acidification process

Secondary acidification is defined as the process by which acid deposition is indirectly accelerated in association with changes in the gas–aerosol partitioning of semi-volatile atmospheric constituents, such as nitric acid, hydrochloric acid, and ammonia, even though emissions of these species and their precursors remain constant.

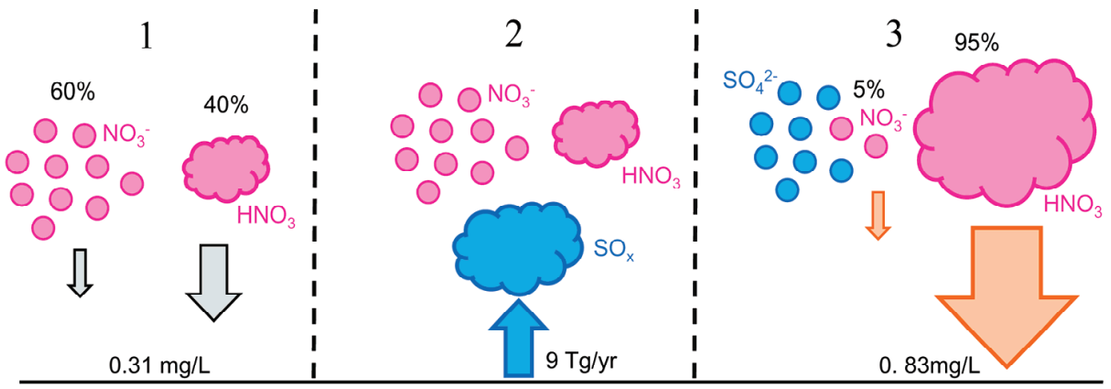

1. Nitric acid is partitioned into HNO_3 gas and NO_3^- aerosol.
   Dry and wet deposition rates of HNO_3 gas are higher than those of NO_3^- aerosol.
2. If SO_2 gas and consequently, H_2SO_4 gas increase, but total (gas + aerosol) nitric acid remain unchanged, then
3. H_2SO_4 quickly forms $(NH_4)_2SO_4$ aerosol, NO_3^- shifts to gas phase, increasing the concentration of HNO_3 gas.
   Consequently, deposition of total nitric acid increases, although total nitric acid concentration remain unchanged.

Fig. 1. Schematic illustration of secondary acidification by nitric acid. Values shown in the figure are those observed during the Miyakejima volcanic eruption event, discussed in section 3.1.

Gas–aerosol equilibrium of semi-volatile inorganic components in solid aerosols	Reaction No.
$NH_3(g) + HNO_3(g) \leftrightarrow NH_4NO_3(s)$	(R1)
$NH_3(g) + HCl(g) \leftrightarrow NH_4Cl(s)$	(R2)
Gas–aerosol equilibrium of semi-volatile inorganic components in liquid aerosols	
$NH_3(g) + HNO_3(g) \leftrightarrow NH_4^+ + NO_3^-$	(R3)
$NH_3(g) + HCl(g) \leftrightarrow NH_4^+ + Cl^-$	(R4)
As sulfuric acid gas increases via photochemical oxidation of SO_2	
$SO_2(g) + OH$ radical $(g) \rightarrow H_2SO_4(g)$	(R5)
$H_2SO_4(g) + NH_3(g) \rightarrow NH_4HSO_4(p)$	(R6)
$H_2SO_4(g) + 2NH_3(g) \rightarrow (NH_4)_2SO_4(p)$	(R7)
As sulfate increases via aqueous-phase oxidation	
$^1S(IV) + O_3(aq) \rightarrow S(VI) + O_2$	(R8)
$HSO_3^- + H_2O_2(aq) \rightarrow SO_4^{2-} + H_2O$	(R9)
$SO_4^{2-} + 2NH_4^+ \leftrightarrow (NH_4)_2SO_4$	(R10)
In the presence of sea-salt particles	
$2NaCl + H_2SO_4(g) \rightarrow Na2SO_4 + HCl(g)$	(R11)
$NaCl + HNO_3(g) \rightarrow NaNO_3 + HCl(g)$	(R12)
In the presence of calcite-rich dust particles	
$CaCO_3 + H_2SO_4(g) \rightarrow CaSO_4 + H_2O + CO_2(g)$	(R13)
$CaCO_3 + HNO_3(g) \rightarrow Ca(NO_3)_2 + H_2O + CO_2(g)$	(R14)

1. S(IV) ≡ $SO_2 \cdot H_2O$, HSO_3^-, and SO_3^{2-}; S(VI) ≡ HSO_4^- and SO_4^{2-}

Table 1. Chemical reactions describing the changes in gas–aerosol partitioning of semi-volatile inorganic components involved in the secondary acidification process.

Figure 1 illustrates schematically secondary acidification effects of nitric acid caused by increases in SO_2 emissions. The values used in Figure 1 are those measured at the Happo Ridge observatory and on Miyakejima Island, and reflect secondary acidification effects due to the eruption of Miyakejima volcano (see section 3.1 for details). Table 1 summarizes typical chemical reactions between atmospheric constituents involved in the secondary acidification process. Nitric acid is partitioned into HNO_3 gas and NO_3^- aerosol in the atmosphere (Figure 1, panel 1; R1 and R3 in Table 1). Since the partitioning is sensitive to temperature, over East Asia the gas phase is dominant in summer and at lower altitude, whereas the aerosol phase is dominant in winter and at higher altitude (Morino et al., 2006; Hayami et al., 2008; Kajino et al., 2008). This partitioning is also altered by the presence of other inorganic components. Hereafter, for simplicity, we focus on thermodynamic equilibrium in the NH_3–HNO_3–H_2SO_4–H_2O system. An increase in SO_2 emissions (Figure 1, panel 2), is followed by the oxidation of SO_2 [S(IV)] to S(VI), that is, either to H_2SO_4 gas by a gas-phase photochemical reaction (R5), or to SO_4^{2-} by aqueous-phase reactions (R8 and R9) in liquid aerosol or rain droplets. Because the vapor pressure of H_2SO_4 gas is extremely low, ammonium sulfate aerosols form immediately (R6 and R7). In the aqueous phase, SO_4^{2-}, because it is a strong acid, forms an ion pair with NH_4^+ (R10). Because sulfate consumes ammonia in the gas phase, the equilibrium of (R1 and R3) shifts leftward, and, as a result, HNO_3 gas evaporates from the aerosol phase (Figure 1, panel 3).

Wet and dry deposition rates of the highly reactive gaseous HNO_3 are high (Seinfeld and Pandis, 2006). Thus, as the SO_4^{2-} concentration increases, the concentration fraction of HNO_3

increases, with the result that deposition of total nitrate (t-NO_3 = HNO_3 + NO_3^-) is enhanced, even though the total nitrate concentration, as well as that of its precursors (i.e., NO_x), remains unchanged.

In the presence of abundant sea salt or mineral dust particles, however, HNO_3 gas is deposited on particle surfaces, expelling Cl^- and CO_3^-, respectively, into the gas phase (R12 and R14). Na^+ from sea salt and Ca^{2+} from mineral dust particles can also be counterions of SO_4^{2-} (R11 and R13). In such cases, increases in the gas phase fraction of t-NO_3 due to increased SO_4^{2-} and subsequent consumption of NH_3 are suppressed (see also section 4.1 and Kajino et al., 2008).

3. Eruption of Miyakejima volcano and the resulting secondary acidification effects in Japan

The eruption of Miyakejima volcano (Mt. Oyama, 139°32′E, 34°05′N, summit elevation 815 m ASL; Figure 2), 180 km south of Tokyo, Japan, beginning in July 2000 has resulted in the emission of huge amounts of sulfur dioxide. The annual mass of sulfur dioxide emitted was vast (9 Tg yr^{-1}; Kajino et al., 2004), equivalent to half the annual anthropogenic emission from China in 2000 (20 Tg yr^{-1}, Streets et al., 2003). Gases, aerosols, and precipitation have been sampled at the Happo Ridge observatory (137°48′E, 36°41′N, 1,850 m ASL, 330 km north of the volcano; Figure 2) in the central mountainous region of Japan since May 1998, two years before the eruption began (Satsumabayashi et al., 2004). Kajino et al. (2004, 2005) used a chemical transport model to simulate the emission, transport, transformation, and deposition of inorganic compounds such as SO_4^{2-}, NO_3^-, and NH_4^+ of anthropogenic and volcanic origin for the one-year period from September 2000 to August 2001. In this section, we highlight the outcomes of our previous research, focusing on the effects of the volcanic eruption on concentrations and deposition of inorganic compounds over the far East Asian region.

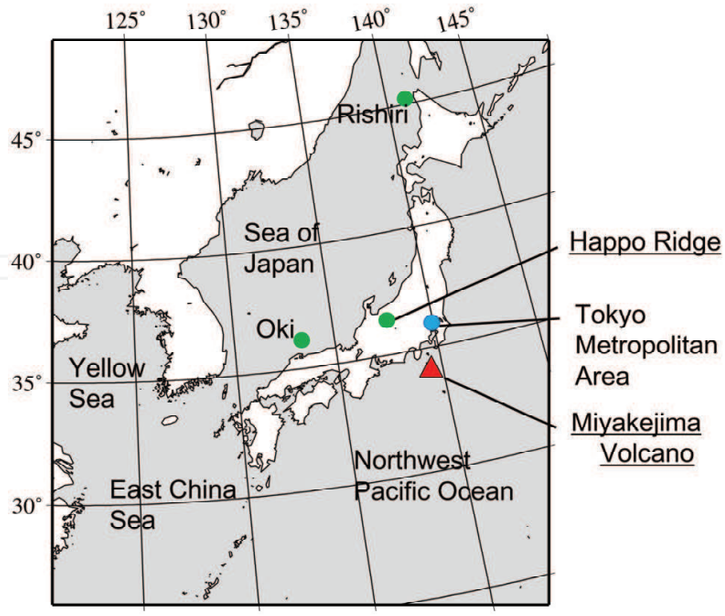

Fig. 2. Map of Japan showing the locations of the Happo Ridge observatory, Miyakejima volcano, the Tokyo Metropolitan Area, and the EANET monitoring stations Oki and Rishiri (see section 4).

3.1 Observational evidence

Temporal variations in smoke height (m) and SO_2 emissions (ton day^{-1}) from Miyakejima volcano (Figure 3) were measured with a correlation spectrometer (COSPEC) by the Japan Meteorological Agency (Kazahaya, 2001). From the start of the observation, total measured SO_2 emissions were 9 Tg yr^{-1}, corresponding to about 70% of the global emissions from volcanoes from the 1970s to 1997 (13 Tg yr^{-1}; Andreas and Kasgnoc, 1998) and to about half the anthropogenic SO_2 emitted from China in 2000 (20 Tg yr^{-1}). The maximum emission, about 82,200 ton day^{-1}, was observed at 10:48 LT on 16 November 2000. This value is equivalent to the anthropogenic emission from all of Asia in 2000 (34.3 Tg yr^{-1}, ~94,000 ton day^{-1}; Streets et al., 2003). The observed smoke height on the same day was only 1,000 m, indicating that almost the entire amount was released into the Planetary Boundary Layer. The emission gradually decreased to about 10,000 ton day^{-1} about 1 year after the onset of eruption. In 2002, the emission was still substantial, at 16.8% of Chinese anthropogenic emissions and 3.8 times Japanese anthropogenic emissions (Kajino et al., 2011). The continuous injection of the volcanic plume containing SO_2 into the Planetary Boundary Layer (i.e., the observed smoke height continued below 2,000 m) necessarily affected surface air quality and environmental acidification over far East Asia substantially.

At Happo Ridge, aerosol samples are collected daily for 3 hours, from 12:00 to 15:00 LT, with a high-volume air sampler. The four-stage filter pack method was used for intensive sampling of gaseous and aerosol inorganic compounds during two weeks in September 1999 and one week in September 2000. Meteorological parameters and hourly concentrations of SO_2, NO_x, O_3, and PM_{10} are monitored automatically. Satsumabayashi et al. (2004) have described the observation methods in detail.

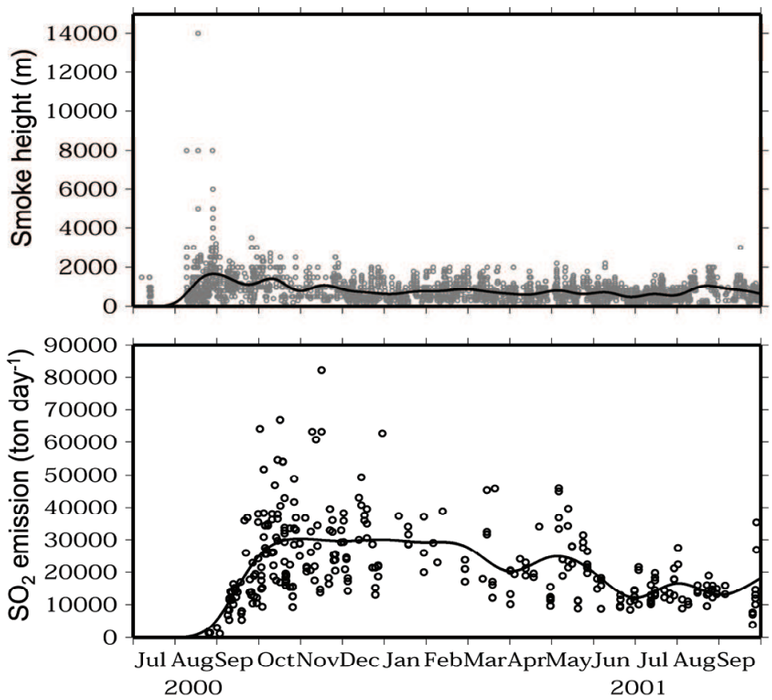

Fig. 3. Time series of observed smoke height (top) and SO_2 emissions (bottom) from Miyakejima volcano. The data were interpolated using a spline function (solid lines) for use as input in the model simulation.

Sampling date and time (LT)	SO_4^{2-} mg m^{-3}	Particle phase fraction	
		Nitrate	Ammonium
	Air mass of Asian continental origin before the eruption (1999)		
13 Sep 12:00–15:00	12.3	0.60	0.78
13 Sep 15:00–18:00	12.1	0.61	0.77
13 Sep 18:00–21:00	8.80	0.57	0.76
13 Sep 21:00–24:00	8.10	0.82	0.72
14 Sep 00:00–03:00	10.7	0.50	0.74
Average	10.4	0.62	0.75
	Air mass directly affected by the volcanic eruption (2000)		
15 Sep 12:00–18:00	32.0	0.00	0.96
15 Sep 18:00–24:00	20.3	0.00	0.94
16 Sep 00:00–06:00	11.0	0.17	0.76
16 Sep 06:00–12:00	6.40	0.00	0.75
Average	17.4	0.04	0.85

Table 2. Gas–aerosol partitioning observed at Happo Ridge before and after the onset of the eruption.

We selected two high sulfate concentration events, from 12:00 LT 13 September to 3:00 LT 14 September 1999, before the onset of the eruption, and from 12:00 LT 15 September to 12:00 LT 16 September 2000, just after the onset of the eruption, and examined SO_4^{2-} concentrations and gas–aerosol partitioning of t-NO_3 and t-NH_4 (= NH_3 + NH_4^+) measured at Happo Ridge (Table 2). Prior to the eruption, in September 1999, the gas–aerosol partitioning of nitrate in the contaminated air mass from the Asian continent tended to favor the aerosol phase: 62% in the aerosol phase versus 38% in the gas phase (Figure 1, panel 1). Similarly, the gas–aerosol partitioning of ammonia also favored the aerosol phase (72% aerosol, 25% gas). In September 2000, two months after the onset of eruption, the gas–aerosol partitioning of nitrate in the air mass from Miyakejima Island was biased almost entirely toward the gas phase (4% aerosol, 96% gas), whereas the aerosol phase fraction of ammonium was higher (85%) than it was before the eruption onset. This result is consistent with thermodynamic equilibrium theory (Table 1).

Table 3 lists the mean bimonthly concentrations of trace chemical components in gases, aerosols, and precipitation measured at Happo Ridge before and after the onset of the eruption. After the eruption, the concentrations of SO_2 gas, SO_4^{2-} aerosol, and SO_4^{2-} in precipitation increased dramatically, by 15, 3, and 6.8 times, respectively, compared with their concentration before the eruption. The concentration of NH_4^+, a major counterion of SO_4^{2-} in aerosols doubled, and it increased in precipitation, by 5 times after the eruption. O_3 and PM_{10} (aerosols smaller than 10μm in diameter) concentrations were slightly higher in September 2000 than before the eruption, but the difference was small compared with the concentration differences in inorganic compounds, indicating that photochemical activity and the total aerosol concentrations were not very different between the period before and that after the eruption began. However, NO_3^- in precipitation increased by 2.7 times after the eruption, whereas aerosol NO_3^- concentrations did not differ between the two periods. Unfortunately, continuous measurement data for HNO_3 gas are not available, so t-NO_3 cannot be determined. Because secondary acidification is defined as an increase in NO_3^- deposition while the t-NO_3 concentration remains unchanged, we cannot prove that the observed increase in bimonthly

mean NO_3^- in rainwater was caused by secondary acidification. Nevertheless, the observations are consistent with secondary acidification theory.

	Gas, ppb		Aerosol, μg m^{-3}				Precipitation, mg L^{-1}		
	SO_2	O_3	PM_{10}	SO_4^{2-}	NO_3^-	NH_4^+	SO_4^{2-}	NO_3^-	NH_4^+
Before eruption (Aug. and Sep. 1999)	0.2	38	14	2.2	0.2	0.75	0.25	0.31	0.06
After eruption (Aug. and Sep. 2000)	3.3	46	17	6.5	0.24	1.56	1.70	0.83	0.33

Table 3. Mean bimonthly concentrations of various components of gases, aerosols, and precipitation measured at Happo Ridge before the onset of the eruption and one year later.

It has still not been proved whether wet scavenging of HNO_3 gas or of NO_3^- aerosol is more efficient. Because Henry's law constant of HNO_3 is extremely large and below-cloud scavenging of aerosols is not very efficient, the below-cloud scavenging coefficient of HNO_3 is several times the size of the aerosol scavenging coefficients (Jylhä, 1999a, 1999b). In-cloud aerosol scavenging is much more efficient because the aerosol particles act as cloud condensation nuclei (CCN). HNO_3 can also dissolve in cloud droplets, however, so it is likely that wet scavenging of HNO_3 is more efficient than that of NO_3 aerosols.
Because no methods are available for quantitative measurement of wet scavenging efficiency, numerical models that incorporate cloud dynamical and microphysical processes must be used to determine the wet scavenging efficiency of HNO_3 compared with that of NO_3 aerosols. However, because such models require many assumptions and several parameterizations, especially for modeled gas–aerosol–cloud interaction processes, the numerical answer includes substantial uncertainty. Thus, the results require careful interpretation. In the next section, the simulation results for secondary acidification effects due to the eruption of Miyakejima Volcano are discussed.

3.2 Model simulations

Kajino et al. (2005) investigated secondary acidification due to the Miyakejima eruption over the one-year period from September 2000 to August 2001 by using a chemical transport model (MSSP, Model System for Soluble Particles; Kajino et al., 2004). They concluded that dry and wet deposition of nitrate increased by 0.2–0.8 and 0.5–4 mg m^{-2} day^{-1}, respectively, over far East Asia on average during the year. However, the MSSP model does not include an aerosol dynamics module, and it assumes thermodynamic equilibrium of semi-volatile inorganic compounds. Therefore, we recently developed a more sophisticated aerosol chemical transport and deposition model, and then used the new model to revisit the volcanic eruption study and examine secondary acidification effects of the plume.
The new aerosol chemical transport model used for the simulation is called Regional Air Quality Model 2. In RAQM2, a simple version of a modal-moment aerosol dynamics model (MADMS; Kajino, 2011) was implemented to achieve a completely dynamical (non-equilibrium) solution for gas-to-particle mass transfer over a wide range of aerosol diameters, from 1 nm to greater than 1 μm. MADMS is unique in that it is capable of solving inter-modal coagulation between two modes with very different log-normal size parameters. To consider a variety of atmospheric aerosol properties, including size, chemical composition, and mixing states, a category approach of the EMTACS (Eulerian

Multiscale Tropospheric Aerosol Chemistry and dynamics Simulator) model (Kajino and Kondo, 2011) is utilized. The Advanced Research WRF (Weather Research and Forecasting) model (version 3.1.1; Skamarock et al., 2008) is used to simulate the meteorological field. Lateral and upper boundary concentrations used for the RAQM2 simulation were hourly concentrations of NO_x, O_x, CO, and volatile organic carbons simulated by a global-scale stratospheric and tropospheric chemical climate model (MRI-CCM2; Deushi and Shibata, 2011). Thus, RAQM2 is a so-called one-way nested model of the global chemistry model. The RAQM2 used Streets et al. (2003)'s anthropogenic emission inventory as well as other sources of aerosol emissions such as biogenic sources, open biomass burning, and wind-generated emissions (dust and sea-salt). The model domain is illustrated in Figure 4. There are 100 × 70 horizontal grids, and the resolution is 60 km with a Lambert conformal conic map projection and a reference latitude/longitude of 35°N/115°E. Vertically, there are 28 layers from the ground to 100 hPa in WRF, and 13 layers from the ground to 10 km in RAQM2, with terrain-following coordinates.

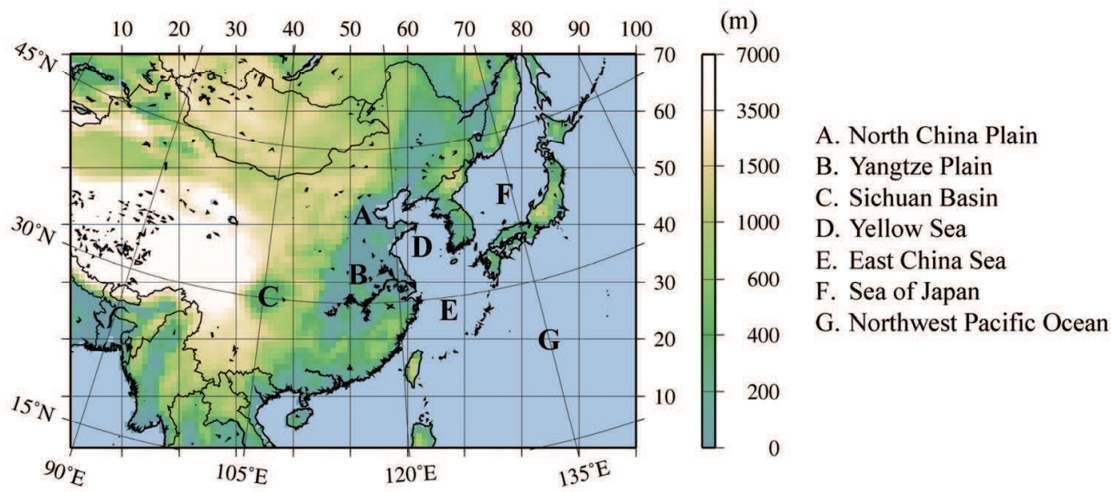

Fig. 4. The WRF and RAQM2 model domain, topography used in the model (color scale, m ASL), and locations of important geographical features.

The simulations were conducted for the month of October 2000. Since wind and precipitation patterns change seasonally, the concentrations and deposition patterns of air pollutants vary substantially during a year. We selected October 2000 for the simulation because during that month volcanic emission was active and the volcanic plume was carried to the Japan archipelago. The Miyakejima volcanic emissions are injected into horizontal grid (X = 87, Y = 39), which corresponds to the location of Miyakejima volcano (Mt. Oyama, 139°32′E, 34°05′N). The SO_2 emission flux and injection height were estimated by spline interpolation of the measured data (solid lines in Figure 3; ~30,000 ton day^{-1}) and uniformly distributed to the vertical grids (Z ≈ 5–7) corresponding to the interval from the summit elevation (815 m ASL) to the measured smoke height (~1,500 m above the crater).

Figure 5 illustrates monthly mean surface concentrations of anthropogenic and volcanic SO_2 and SO_4^{2-} (volcanic data were derived by subtracting the simulation result obtained without including volcanic emissions from that obtained with volcanic emissions), the gas-phase fraction of t-NO_3, and its increase due to increased volcanic SO_4^{2-} in October 2000. The volcanic SO_2 concentration over the area downwind of the volcano (Figure 5b) was

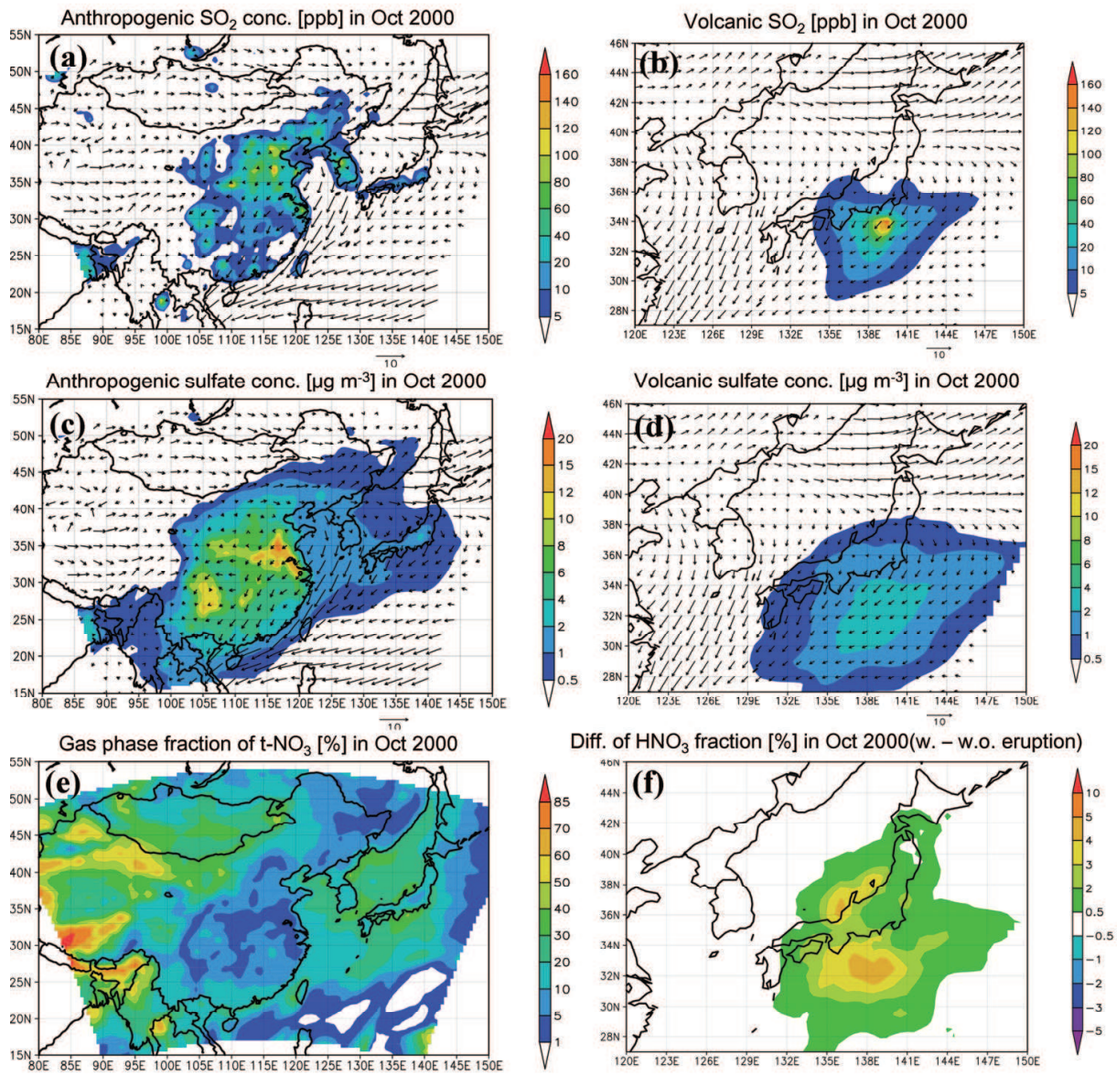

Fig. 5. Spatial distributions of anthropogenic (a and c) and Miyakejima volcanic (b and d) monthly mean surface concentrations of (a and b) SO_2 (ppb) and (c and d) SO_4^{2-} (μg m^{-3}). (e) The gas-phase fraction of t-NO_3 (%) and (f) its increase due to the volcanic eruption (%) in October 2000.

comparable to the anthropogenic SO_2 concentration over the continent, whereas the anthropogenic concentration over Japan was much less (Figure 5a). Because SO_4^{2-} is produced by oxidation of SO_2 during transport, SO_4^{2-} is widely distributed over the downwind areas (Figures 5c and 5d). The maximum concentration of volcanic SO_4^{2-} was smaller than that over the land, probably because photochemical oxidants such as OH radicals, O_3, and H_2O_2 are more abundant over the continent. In central Japan, the SO_4^{2-} concentration was doubled as a result of the volcanic eruption. The gas phase fraction of t-NO_3 was smaller over the continent (1–15%) than over the ocean or the Japan archipelago (20–40%) (Figure 5e), because the surface temperature is higher over the ocean than over the continent in October. These values are consistent with those observed at Happo Ridge. Expulsion of NO_3^- from the aerosol phase occurred as a result of the volcanic SO_2 emission,

with an increase of the gas-phase fraction of about 2–5% (Figure 5f). The gas-phase fraction is small compared with the observed fraction at Happo Ridge, where the gas-phase fraction reached 100% during volcanic plume transport events. It is probably because simulated ammonia concentration is overestimated so that it fixed HNO_3 in the aerosol phase and inhibited the expulsion of NO_3^- due to increased sulfate.

Figures 6a-d illustrates the monthly cumulative dry and wet deposition of t-NO_3 in October 2000 and changes due to the volcanic eruption. Figures 6e and 6f show monthly precipitation over East Asia and around Japan, respectively. Secondary acidification in dry deposition, that is, the increase of nitrate in dry deposition, in the region downwind of the Miyakejima volcano, is evident (0.5–3 mg m^{-2}) accounting for at maximum about 10% of the total amount (20–80 mg m^{-2}).

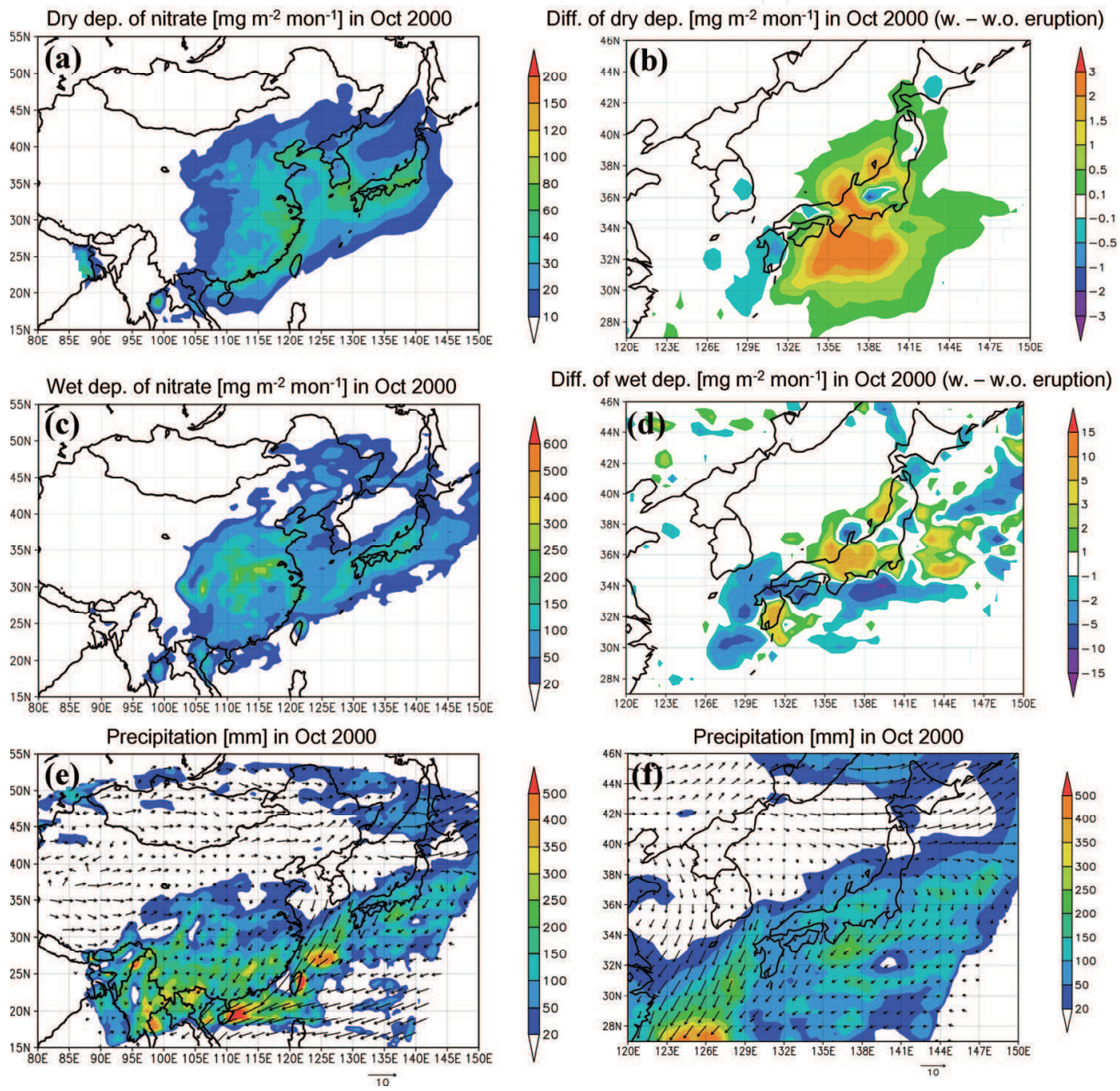

Fig. 6. Spatial distributions of cumulative monthly dry deposition of (a) total nitrate (gas + aerosol) (mg m^{-2}) and (b) the difference due to the eruption. (c and d) The same as (a) and (b) but for wet deposition (mg m^{-2}). (e and f) Monthly cumulative precipitation (mm) in October 2000.

Secondary acidification due to wet deposition was rather complex. An increase in nitrate in wet deposition was simulated over the central Japan land mass (5–10 mg m^{-2}), whereas a decrease of 2–15 (mg m^{-2}) was simulated over the ocean south of the archipelago, where precipitation was heavier. The decrease is due probably to dominance of in-cloud scavenging of aerosols (NO_3^- acting as CCN) over the dissolution of HNO_3 gas, so that the increased fraction of HNO_3 resulted in a decrease in the wet deposition of t-NO_3.The modeled wet deposition increase was smaller than that predicted by MSSP (15–120 mg m^{-2}), which simulated that an increase in the wet deposition of nitrate was comparable to that of sulfate (see Area 1, October 2000 in Table 3 of Kajino et al., 2005).

Even though the RAQM2 model is more sophisticated than the MSSP model, it is hard to judge which model results are closer to reality. MSSP does not solve aerosol processes dynamically. The aerosol size distribution is diagnosed as a simple function of relative humidity, and all particles of inorganic compounds such as SO_4^{2-}, NO_3^-, and NH_4^+ are assumed to act as CCN and to become dissolved in cloud droplets (Kajino et al., 2004). In contrast, the more sophisticated RAQM2 model solves the evolution processes (condensation, evaporation, and coagulation) of the aerosol size distribution dynamically for aerosol diameter ranges from 1 nm to greater than 1 μm. Then, the CCN activity of particles is calculated using the parameterization of Abdul-Razzak and Ghan (2000). This parameterization was developed from cloud parcel model calculations, including aerosol–cloud interaction processes. The critical diameter D_c (above which aerosol particles can act as CCN) is calculated from the predicted aerosol size distribution and chemical composition, the temperature and humidity in the environment, and the updraft velocity. Ironically, however, because it is quite challenging to reproduce atmospheric aerosol size distributions, especially for sub-micron particles, RAQM2 can fail to reproduce the CCN activity of aerosols, which is very sensitive to particle size. Nevertheless, the simulated results of the two models should not be far from reality, as the model results for various concentrations of inorganic components in the air and in precipitation have been evaluated extensively using measurement data (Kajino et al., 2011, and references therein; Kajino and Kondo, 2011).

4. Secondary acidification as a result of long-range transport over East Asia

In section 3, we showed that secondary acidification occurred during an extreme episode. In this section, we investigate secondary acidification under general air pollution conditions. Asia is one of the largest anthropogenic SO_x emitting regions in the world, and because of the rapid economic growth in Asia, emissions there might change drastically in the future. Therefore, understanding the impacts of secondary acidification in regions downwind of large emission sources and how they change depending on future emission changes is important. In section 4.1, we present indications of secondary acidification based on Acid Deposition Monitoring Network in East Asia (EANET) data. In section 4.2, we use a chemical transport model to simulate long-range transport of inorganic air pollutants over the East Asian region. To evaluate the secondary acidification due to future emission changes, we carried out simple sensitivity studies by increasing or decreasing emissions of SO_2 and NH_3, the gaseous counterparts of SO_4^{2-} and NO_3^- aerosols, in model simulations.

4.1 Observational evidence

We found indications of secondary acidification in the EANET monitoring data. EANET began collecting data on a regular basis in 2001, following established guidelines and technical

procedures and adopting a quality assurance/quality control program (EANET, Guidelines for Acid Deposition Monitoring in East Asia; available from http://www.eanet.cc/product.html). In 2002, two additional Japanese monitoring stations began to measure concentrations of gas and aerosol components by the filter pack (FP) method, increasing the number of monitoring stations in Japan to the current 10. At these stations, 7- or 14-day cumulative concentrations of gaseous species (HNO_3, HCl, NH_3, SO_2) and aerosol components (SO_4^{2-}, NO_3^-, Cl^-, NH_4^+, Na^+, Mg^{2+}, K^+, Ca^{2+}) are monitored, and 1-day cumulative concentrations in precipitation (SO_4^{2-}, NO_3^-, Cl^-, NH_4^+, Na^+, Mg^{2+}, K^+, Ca^{2+}) are measured by collecting precipitation samples and analyzing them by ion chromatography.

The FP method is known to have several distinct artifact problems. Because particulate NH_4NO_3 and NH_4Cl collected on a filter might volatilize during a 7- or 14-d sampling period, there is a possibility that thermodynamic equilibrium may not have been attained. In addition, high humidity can reduce the concentration of gaseous species because of trapping by condensed water in the filter pack. To evaluate these sampling artifacts in the EANET FP data, we employed a multicomponent gas–aerosol equilibrium model called Simulating Compositions of Atmospheric Particles at Equilibrium (SCAPE; Kim et al., 1993; Meng et al., 1995) to recalculate the gas–aerosol partitioning of t-NO_3 at six selected Japanese EANET monitoring sites and compared the results with the measurement data (Kajino et al., 2008). We found fairly high correlations, low mean errors, and low root mean square errors between the observed and simulated values (see Table 2 of Kajino et al., 2008). We therefore concluded that long-duration FP data from EANET are sufficiently consistent for detecting the secondary acidification effect in our current analysis.

In the present study, we used monitoring data collected by two of the Japanese EANET stations, Rishiri and Oki. As shown in Figure 2, these stations are situated on small islands facing the Sea of Japan, so plumes from the continental outflow are efficiently detected. Rishiri is further north than Oki, so the climate and air quality features differ between these two stations.

Table 4 summarizes the monitoring results from Oki and Rishiri. Non-sea-salt (nss)-SO_4^{2-}, defined as the concentration difference between total [SO_4^{2-}] and sea-salt-originated SO_4^{2-} (= 0.251 × [Na^+]) consists mostly of anthropogenic and partly of volcanic sulfate. Here, the square brackets [ ] denote atmospheric concentration (μg m^{-3}). $C_{nssS/N5}$ is the molar ratio of nss-SO_4^{2-} to the N(V) concentration, namely t-NO_3, where C denotes the atmospheric concentration. P_{gHNO3} is the molar fraction of HNO_3 gas relative to t-NO_3. F_s, defined as,

$$F_s \equiv \frac{S(IV)}{S(IV)+nssS(VI)} = \frac{[S]_{SO_2}}{[S]_{SO_2}+[S]_{nss-SO_4^{2-}}} \quad (1)$$

is the ratio of tetravalent *S* to total (tetravalent plus hexavalent) anthropogenic *S* in the air. Under the assumption that all SO_2 is of non-sea-salt origin, a low F_s value indicates that SO_2 is sufficiently oxidized to SO_4^{2-} during long-range transport. $D_{N5/S6}/C_{N5/S6}$ is the ratio of the N/S molar ratio in precipitation to the atmospheric ratio (where D indicates wet deposition):

$$D_{N5/S6} / C_{N5/S6} \equiv \frac{d[NO_3^-]}{d[SO_4^{2-}]} \times \frac{[SO_4^{2-}]_p / 96}{[HNO_3]_g / 63 + [NO_3^-]_p / 62} \quad (2)$$

Here, *d[ ]* denotes the concentration in precipitation (μmol L^{-1}), and the subscripts *g* and *p* denote the gas phase and the particulate phase, respectively. As atmospheric concentrations

were measured by the FP method on a 7- or 14-d cycle, the daily measured wet deposition amounts are also averaged over the same sampling period.

Station name	Oki			Rishiri		
Observation period	04/2003 – 03/2005			07/2002 – 03/2005		
Number of samples	77			72		
Longitude/Latitude	133.18/36.70			141.20/45.12		
	Mean concentration ± standard deviation, μg m^{-3}					
[nss-SO_4^{2-}]	3.54	±	2.05	1.86	±	0.95
[t-NO_3]	1.21	±	0.61	0.73	±	0.47
[t-NH_4]	1.26	±	0.77	0.68	±	0.34
[Crustals] [a]	2.64	±	1.58	2.31	±	1.26
	Mean meteorological measurements with standard deviations					
T, °C	14.48	±	7.17	6.50	±	8.72
RH, %	74.10	±	6.16	75.69	±	6.00
	Mean molar ratios with standard deviations					
[nss-SO_4^{2-}]/[SO_4^{2-}]	0.86	±	0.11	0.78	±	0.13
$C_{nssS/N5}$	1.99	±	1.06	1.96	±	1.00
P_{gHNO3}	0.30	±	0.22	0.20	±	0.16
F_s	0.37	±	0.16	0.34	±	0.14
	Correlation coefficient (*R*)					
T versus P_{gHNO3}	0.63			0.46		
$C_{nssS/N5}$ versus P_{gHNO3} [b]	0.75			–0.03	→	0.41
P_{gHNO3} versus $D_{N5/S6}/C_{N5/S6}$ [b]	0.74			0.17	→	0.70
F_s versus $D_{N5/S6}/C_{N5/S6}$ [b]	–0.45			0.08	→	–0.43

[a][Crustals] = [Na^+] + [Mg^{2+}] + [K^+] + [Ca^{2+}]

[b]The correlation coefficient *R* at Rishiri improved when it was calculated using only data collected when [nss-SO_4^{2-}]/[SO_4^{2-}] > 0.8 and T > 0 °C .

Table 4. Information about Oki and Rishiri stations and monitoring results.

In general, Rishiri and Oki can be characterized as follows. Rishiri is located in northern Japan where temperatures drop to below 0 °C in winter and the marine atmosphere is relatively clean. Thus, the mean anthropogenic indicator [nss-SO_4^{2-}]/[SO_4^{2-}] was lower than 0.8. As the counterions of NO_3^-, sea-salt-originated crustal concentrations of Na^+ and Mg^{2+} were high (>2 μg m^{-3}), resulting in a low P_{gHNO3} (0.2) value. In contrast, Oki is located in coastal western Japan, where it is influenced by Asian continental outflows, resulting in relatively higher values of [nss-SO_4^{2-}]/[SO_4^{2-}] (>0.85) and P_{gHNO3} (0.3). Relative humidity (RH) did not differ significantly between the two stations.

Measured P_{gHNO3} was positively correlated with T, as explained in section 2. We found a slightly larger correlation between P_{gHNO3} and $C_{nssS/N5}$ at Oki in western Japan, indicating a marked expulsion of NO_3^- by SO_4^{2-} in the continental outflow. Conversely, at Rishiri the correlation coefficient between P_{gHNO3} and $C_{nssS/N5}$ was near zero, which we attributed to the effects of abundant sea-salt components (R12). P_{gHNO3} and $D_{N5/S6}/C_{N5/S6}$ were positively correlated at Oki. Here, $D_{N5/S6}/C_{N5/S6}$ represents the N(V)/S(VI) molar concentration ratio

in precipitation to that in the atmosphere (Eq. 2). Accordingly, a positive correlation between P_{gHNO3} and $D_{N5/S6}/C_{N5/S6}$ indicates a relatively higher wet deposition rate of t-NO_3, compared with that of S(VI), as the gas phase fraction of t-NO_3 increases, that is, secondary acidification. Together with the positive correlation between $C_{nssS/N5}$ and P_{gHNO3}, the expulsion of particulate NO_3^- to the gas phase by anthropogenic SO_4^{2-} results in acceleration of the wet deposition flux of t-NO_3 at Oki.

At Rishiri, where no correlation was detected between $C_{nssS/N5}$ and P_{gHNO3}, analysis on the basis of the $D_{N5/S6}/C_{N5/S6}$ ratio is not applicable. Because of the abundance of cations of sea-salt origin, the correlation coefficient between P_{gHNO3} and $D_{N5/S6}/C_{N5/S6}$ is 0.17. In addition, the secondary acidification effect is usually based on the calculation of the vapor–liquid equilibrium of semivolatile components, but Rishiri station is in northern Japan, where precipitation during winter consists mostly of ice and snow rather than rain. Therefore, we selected data sampled when the mean temperature exceeded 0 °C and [nss-SO_4^{2-}]/[SO_4^{2-}] was greater than a threshold of 0.8, indicating less influence of sea-salt particles. The same analysis using the selected samples resulted in an increase in the correlation coefficient between $C_{nssS/N5}$ and P_{gHNO3} from –0.03 to 0.41, and that between P_{gHNO3} and $D_{N5/S6}/C_{N5/S6}$ increased from 0.17 to 0.70. Secondary acidification is thus evident under the substantial influence of anthropogenic contamination when the influence of sea-salt particles is low and the temperature is sufficiently high for vapor–liquid equilibrium to be established. Neutralization effects by the Asian dust particles (R14) may negate the increase in P_{gHNO3} caused by the increase in SO_4^{2-}. We thus performed a similar analysis using [nss-Ca^{2+}]/[Ca^{2+}], but found no significant effects in the current data sets. Here, [nss-Ca^{2+}] is defined as the difference between total [Ca^{2+}] and sea-salt-originated Ca^{2+} (= 0.038 [Na+]); therefore, higher values of [nss-Ca^{2+}]/[Ca^{2+}] would indicate the occurrence of Asian dust events, which are characterized by abundant calcite.

Figure 7 shows the relationships between $C_{nssS/N5}$ and $P_{g\text{-}HNO3}$ (%), $P_{g\text{-}HNO3}$ (%) and $D_{N5/S6/CN5/S6}$, and F_s and $D_{N5/S6/CN5/S6}$ at Oki and Rishiri. At Oki, the correlations are higher because of its location in western Japan where it is influenced by the pronounced Asian continental outflow. At Rishiri, however, the sea-salt effect is predominant, leading to very weak correlations (open circles in Figs. 7d–f), although they are enhanced significantly by sample selection for T > 0 °C and [nss-SO_4^{2-}]/[SO_4^{2-}] > 0.8 (closed circles).

It is notable that the regression lines obtained from the two stations are very similar despite the ~1,200 km distance separating them. P_{gHNO3} is less than 30% when $C_{nssS/N5}$ is less than 2 at Oki (Fig. 7a), whereas P_{gHNO3} is often greater than 50% under the lower influence of sea-salt particles (closed circles) when $C_{nssS/N5}$ is less than 2 at Rishiri (Fig. 7d). The slope of this regression line for Rishiri is steeper than that for Oki, because the average concentration of t-NH_4, which can fix NO_3^- as ammonium nitrate in the aerosol phase, is low at Rishiri, only half the average concentration at Oki. However, when cations originating from sea salt are abundant at Rishiri (open circles in Figure 7d), P_{gHNO3} is less than 20%, even when $C_{nssS/N5}$ is larger than 4.

The F_s value is an indicator of the distance that pollutants have been transported. Relatively short-distance transport within Japan is indicated by an F_s value greater than approximately 0.6. Conversely, F_s smaller than 0.2 indicates long-range transport from the Asian continent to Japan (Satsumabayashi et al., 2004). At Oki, $D_{N5/S6/CN5/S6}$ was greater than 3 when F_s was smaller than 0.2 (Fig. 7c), indicating that secondary acidification effects were greater at Oki when air pollutants had been transported a long distance. The same trend was observed for the selected samples at Rishiri (closed circles, Fig. 7f).

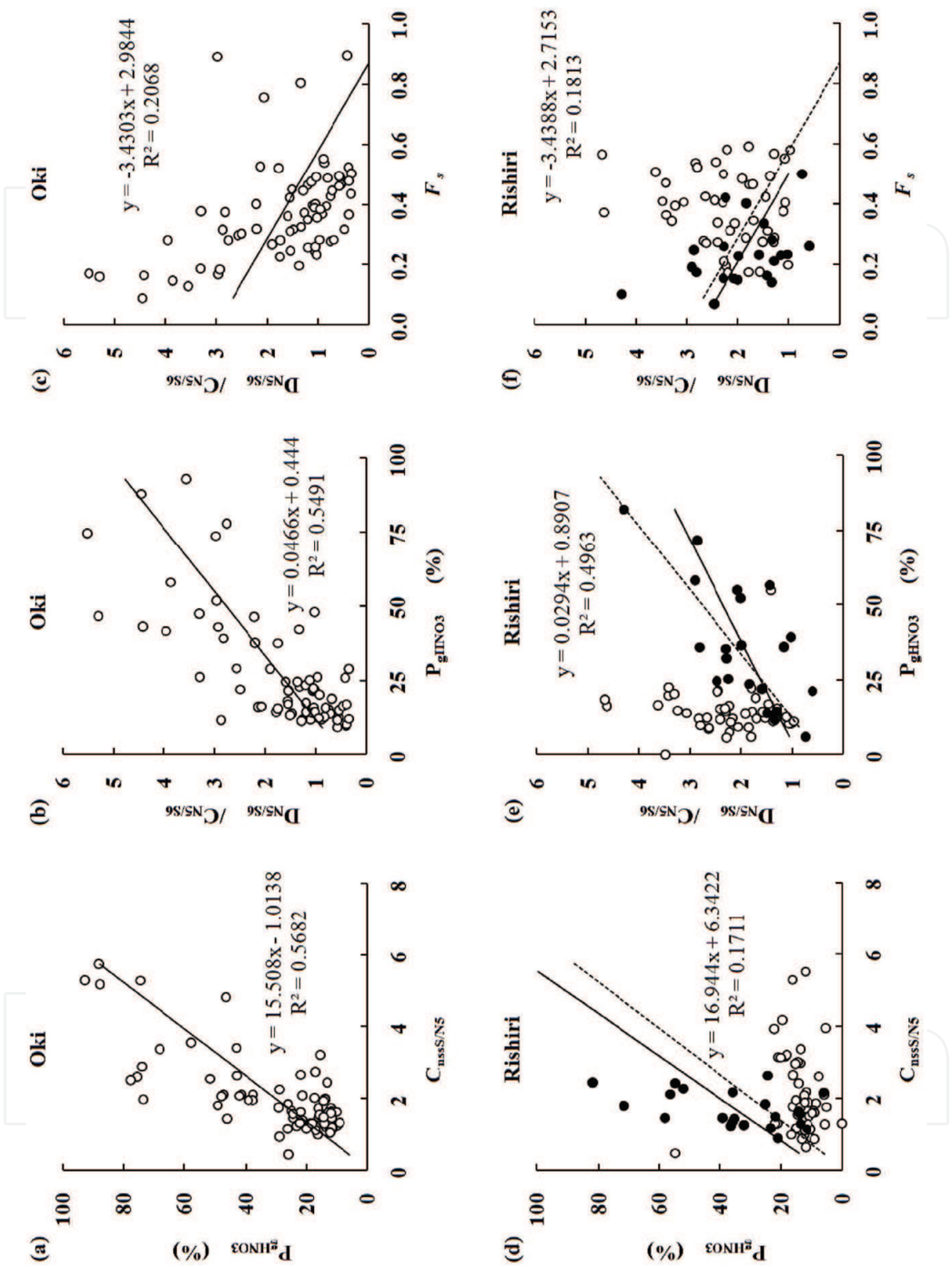

Fig. 7. Scattergrams of (a) $C_{nssS/N5}$ and P_{gHNO3}, (b) P_{gHNO3} and $D_{N5/S6}/C_{N5/S6}$, (c) F_s and $D_{N5/S6}/C_{N5/S6}$ at Oki. (d–f) Same as (a–c) for Rishiri. The open circles in (a–f) show all data. The closed circles in (d–f) show data of samples collected when T > 0 °C and [nss-SO_4^{2-}]/[SO_4^{2-}] > 0.8. The solid regression lines in (d–f) are for all data, and the dashed regressions lines are for only the data shown by the closed circles.

4.2 Model simulations

4.2.1 Future emission scenarios

In all four scenarios (A1, A2, B1, and B2) considered in the Special Report on Emissions Scenarios (SRES) from the Intergovernmental Panel on Climate Change (IPCC) (2000), emission rates are increasing faster in Asia than elsewhere in the world. In these scenarios, SO_x emissions in Asia are expected to peak between 2020 and 2050, becoming twice as high as in 2000. NO_x emissions will continue to increase even when SO_x is no longer increasing, reaching a maximum after 2040 at levels more than twice current levels in the lowest estimation scenario (B1), and in the A2 scenario reaching a level approximately four times the current level in 2100. SRES does not evaluate NH_x emission rates, which have a marked effect on gas–aerosol partitioning, but Klimont et al. (2001) estimated that NH_x emissions will increase to 1.7 times the 1995 level in East Asia by 2030.

Fujino et al. (2002) developed the AIM/Trend model (Asian-Pacific Integrated Model) to assess future environmental loads based on past socio-economic trends. They estimated a change in Asian SO_2 emissions from 30.8 Tg yr^{-1} in 1998 to 21.9–85.1 Tg yr^{-1} in 2032, depending on the socio-economic scenario, Security First (SF), Market First, Sustainability First, or Policy First. The largest emission growth ratio is estimated for the SF scenario, which assumes a world of great disparities where inequality and conflict brought about by socio-economic and environmental stresses will prevail. In that scenario, SO_2 emission in China is predicted to grow to 2.42 times the 2000 level by 2030 (Kajino and Ueda, 2007).

Representative Concentration Pathways (RCPs) are new future emission scenarios that have recently been provided as part of the Coupled Model Intercomparison Project Phase 5 (http://cmip-pcmdi.llnl.gov/cmip5) prepared for the Fifth Assessment Report (AR5) of the IPCC, which is scheduled to be published in 2013. The current version of the RCP database (version 2.0.5) is available at http://www.iiasa.ac.at/web-apps/tnt/RcpDb/. The four RCP future emission scenarios are RCP 3-PD (IMAGE, van Vuuren et al., 2007), RCP 4.5 (MiniCAM; Clarke et al., 2007), RCP 6.0 (AIM; Fujino et al., 2006; Hijioka et al., 2008), and RCP 8.5 (MESSAGE, Riahi et al., 2007). The RCP 2.0.5 emission scenarios for the period until 2050 predict that total Asian SO_2 emissions will increase from 32.4 Tg yr^{-1} in 2000 to as high as 46.3 Tg yr^{-1} (1.43 times; RCP 8.5) in 2020 and then decrease to as little as 12.5 (a 38.6% reduction; RCP 3-PD) in 2050. Total NO_x emissions will increase from 26.3 Tg NO_2 yr^{-1} in 2000 to a high as 48.1 Tg NO_2 yr^{-1} (1.83 times; RCP 8.5) in 2020 and decrease to as little as 25.4 Tg NO_2 yr^{-1} (a 96.6% reduction; RCP 4.5) in 2050. Total Asian NH_3 emissions will increase from 20.9 Tg yr^{-1} in 2000 to as high as 32.7 Tg yr^{-1} (1.56 times; RCP 3-PD), with the minimum predicted value being an increase to 25.6 Tg yr^{-1} (1.22 times; RCP 4.5).

4.2.2 Secondary acidification due to future emissions changes

To investigate secondary acidification effects due to future emissions changes, we performed simple sensitivity studies by simulating increased or decreased emissions of SO_2 and NH_3, the gaseous counterparts of SO_4^{2-} and NO_3^- aerosols (Table 5). The control run (CNTRL) used Regional Emission inventory in ASia (REAS; Ohara et al., 2007) data for 2005 (Kurokawa et al., 2009). The values in Table 5 are the ratio to the CNTRL emissions and were applied uniformly over the whole model domain.

"S2" and "Sh" indicate double and half the SO_2 emission of the CNTRL run, and "NH2" and "NHh" indicates double and half the NH_3 emission of the CNTRL run. We expected secondary acidification effects to be greatest in the S2NHh run, in which SO_2 was increased and the counterpart of NO_3^- was decreased, and that they would be least in the ShNH2 run.

The model (MRI-CCM2-WRF-RAQM2) and the model settings used for these sensitivity studies were identical to those described in section 3.2, except 90 × 60 horizontal grids were

used with the reference latitude/longitude being 37°N/123°E (the model domain is not shown as it is not very different from that shown in Figure 4). The simulation was conducted for March 2006. In spring in East Asia, considerable long-range transport occurs because cyclones and anti-cyclones propagating eastward carry contaminated air masses by turn in cycles of about 5 days.

RUN	CNTRL	S2	S2NHh	Sh	ShNH2
SO_2 emission	1	2	2	0.5	0.5
NO_x emission	1	1	1	1	1
NH_3 emission	1	1	0.5	1	2

Table 5. Ratios of emissions to that of CNTRL run used for sensitivity studies to evaluate secondary acidification due to future emission changes.

Figure 8 illustrates the simulated (CNTRL) spatial distributions of the SO_2 and NO_x emission fluxes and monthly mean surface concentrations of SO_4^{2-} and t-NO_3 in March 2006. SO_2 and NO_x emissions peaks are seen in large emission source regions, and SO_4^{2-} and t-NO_3 are transported widely to southward and eastward downwind regions.

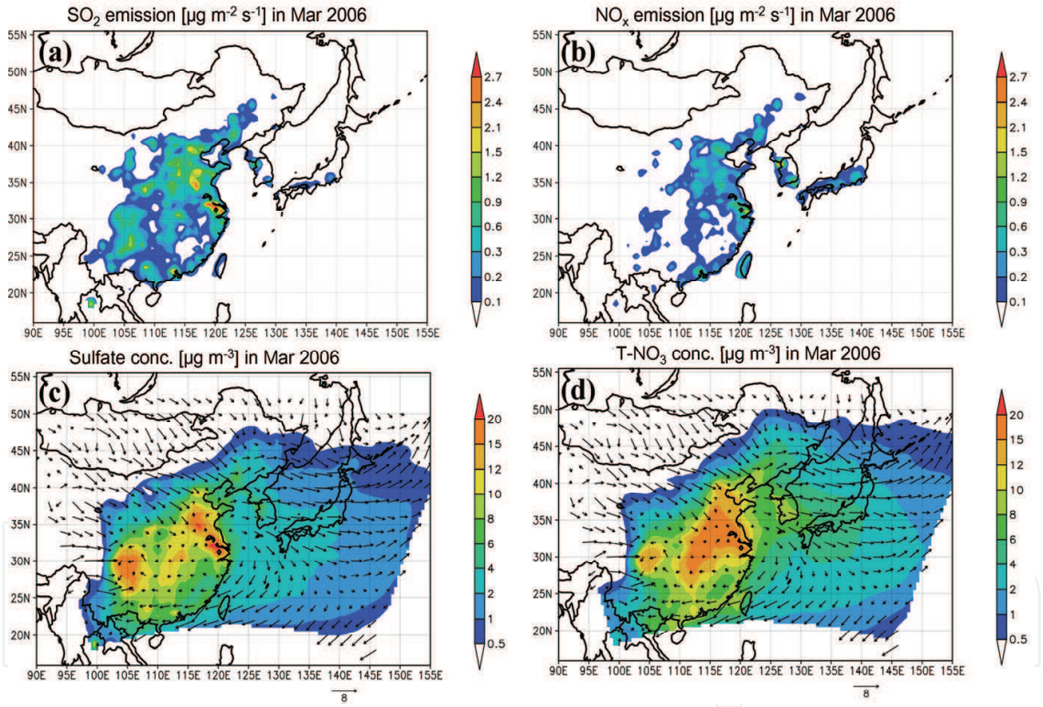

Fig. 8. The simulated (CNTRL) spatial distributions of (a) the SO_2 emission flux (μg m^{-2} s^{-1}), (b) the NO_x emission flux (μg m^{-2} s^{-1}), (c) the monthly mean surface sulfate concentration (μg m^{-3}), and (d) the monthly mean surface total (gas + aerosol) nitrate concentration (μg m^{-3}) in March 2006.

Figure 9 illustrates the simulated (CNTRL) spatial distributions of the gas phase fraction of nitrate, the monthly accumulated precipitation, and the monthly accumulated dry and wet deposition of t-NO_3. The gas phase fraction is larger over the ocean (20–40%) than over the continent (1–30%) because the surface temperature is higher over the ocean in spring. Also because of temperature differences, the gas phase fraction over the land is larger in the south

(5–30%) than in the north (1–5%). The monthly mean surface temperature over the ocean ranges over about 5–20 °C, whereas it ranges from –20 to 0 °C over the northern continent, and from 0 to 15 °C over the southern continent (not shown). In general, the dry deposition amount and the surface concentration are expected to correlate with each other given a relatively constant dry deposition rate. However, the dry deposition amounts are larger over the southern edge of the continent and western Japan, whereas the surface concentrations are larger over the North China Plain, the Sichuan Basin, and the Yangtze Plain. The horizontal distribution of the dry deposition is rather similar to that of the gas phase fraction, because the modeled dry deposition velocities of HNO_3 gas (0.9–2.7 cm s^{-1}) are much larger than those of NO_3^- aerosols (0.02–0.1 cm s^{-1} over the land, 0.2–1 cm s^{-1} over the ocean). The wet deposition amounts are large where both the precipitation and the concentrations are large, and they are about twice to three times the dry deposition amounts.

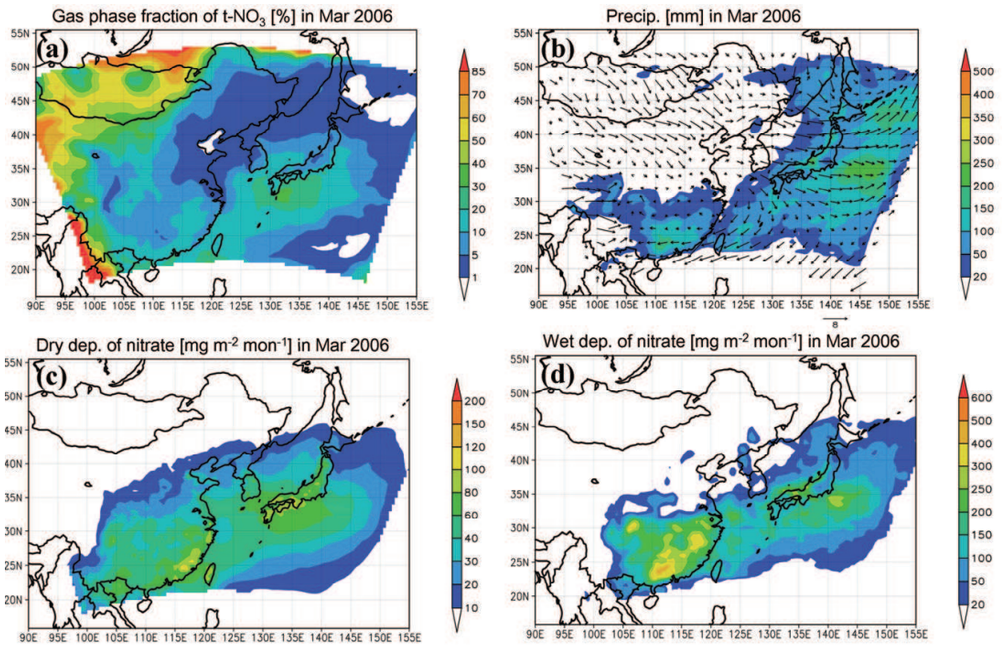

Fig. 9. Spatial distributions of (a) the gas phase fraction of nitrate (%), (b) monthly accumulated precipitation (mm) with surface wind vectors (m s^{-1}), (c) monthly dry deposition amount of nitrate (μg m^{-2} mon^{-1}), and (d) wet deposition of nitrate (μg m^{-2} month) in March 2006.

Figure 10 illustrates the gas phase fraction of nitrate and monthly accumulated total (dry + wet) deposition of t-NO_3 in the CNTRL run and the deviations from the control in the S2 and the S2NHh runs. Doubling SO_2 emissions causes the gas phase fraction to increase by 1–6% over southern China and over the ocean (Figure 10c and d). The increase of the gas phase fraction over northern China is less than 1%, however, because of the low temperatures there. In general, because the East Asian atmosphere is ammonia-rich and is sodium-rich over the ocean, so the expulsion of NO_3^- to the gas phase is not very significant. However, gas phase fraction, of as large as 20% over northern China, is seen, because the counterpart of NO_3^- is decreased substantially. As a result of the increase in the gas phase fraction, the total deposition of nitrate increases by about 5–20 mg m^{-2}, corresponding to about 10% of the total deposition in CNTRL (50–300 mg m^{-2}), when SO_2 emissions double. The increase is larger than 20 mg m^{-2} over wide areas when NH_3 emission is halved, accounting for as much as 50% of the total nitrate of the CNTRL.

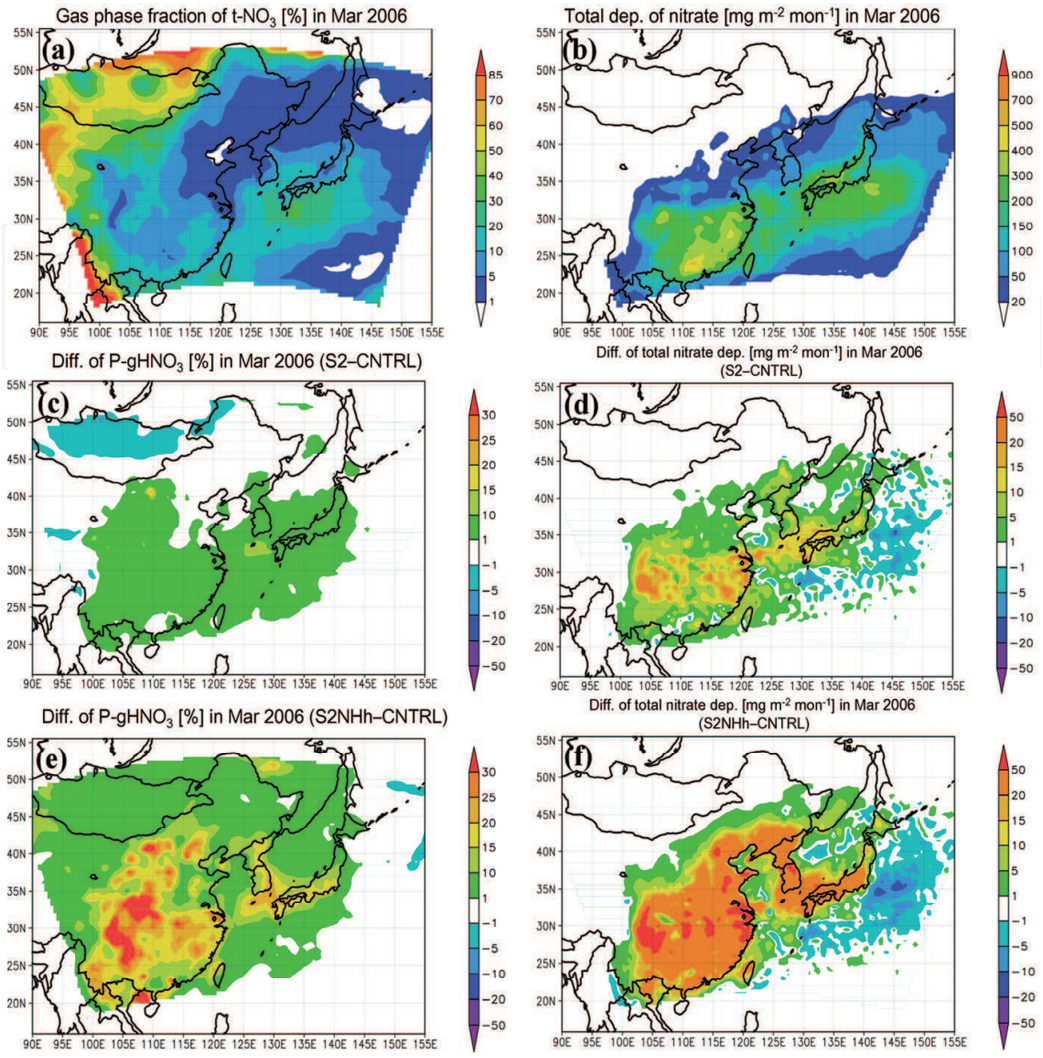

Fig. 10. Spatial distributions of (left panels) gas phase fraction of nitrate (%) and (right panels) total (dry plus wet) deposition of nitrate (μg m^{-2} mon^{-1}). The top panels show the when NH_3 emissions are halved (bottom panels), a pronounced increase in the CNTRL run results and the middle and bottom panels show the results for the differences between the S2 and CNTRL runs (middle) and between the S2NHh and CNTRL runs (bottom).

In contrast, wet plus dry deposition decreases over the Pacific Ocean east of the Japan archipelago by about 1–10 mg m^{-2} in the S2NHh run, probably because the increase in deposition over the downwind regions (the continent and the ocean close to the continent) causes the concentration over the regions further downwind to decrease. Consequently, nitrate deposition also decreases in the regions further downwind.

As discussed before in Sections 3.1 and 3.2, the wet deposition efficiencies of HNO_3 gas and NO_3^- aerosol cannot be directly compared with each other because NO_3^- aerosol particles can act effectively as CCN. When cloud production and NO_3^- aerosol activation are very efficient, secondary acidification may not occur. In contrast, when mature clouds are present and the gravitational fall of rain droplets is dominant, HNO_3 gas is more efficiently captured by water droplets and secondary acidification may occur. The RAQM2 model can show the

quantitative results of secondary acidification due to wet deposition, and the simulation results should not differ much from reality because the model results for the concentrations of inorganic components in the air as well as for precipitation have been evaluated extensively with measurement data. However, in the current off-line coupled WRF-RAQM2 framework, processes related to wet deposition, such as aerosol activation, cloud dynamics, and cloud microphysics, are based on many assumptions and various parameterizations. Thus, it is still not possible to determine whether wet scavenging of HNO_3 gas or of NO_3^- aerosol is in reality more efficient.

4.2.3 Adverse effects of an SO_2 emission decrease: a decrease in nitrate deposition downwind may cause an increase in deposition even further downwind

The widespread installation of flue-gas desulfurization (FGD) devices is expected to decrease Asian SO_2 emissions in the future. In China, FGD devices are now being installed in many coal-fired power plants. From 2001 to 2006, FGD penetration increased from 3% to 30%, causing a 15% decrease in the average SO_2 emission factor of coal-fired power plants (Zhang et al., 2009).

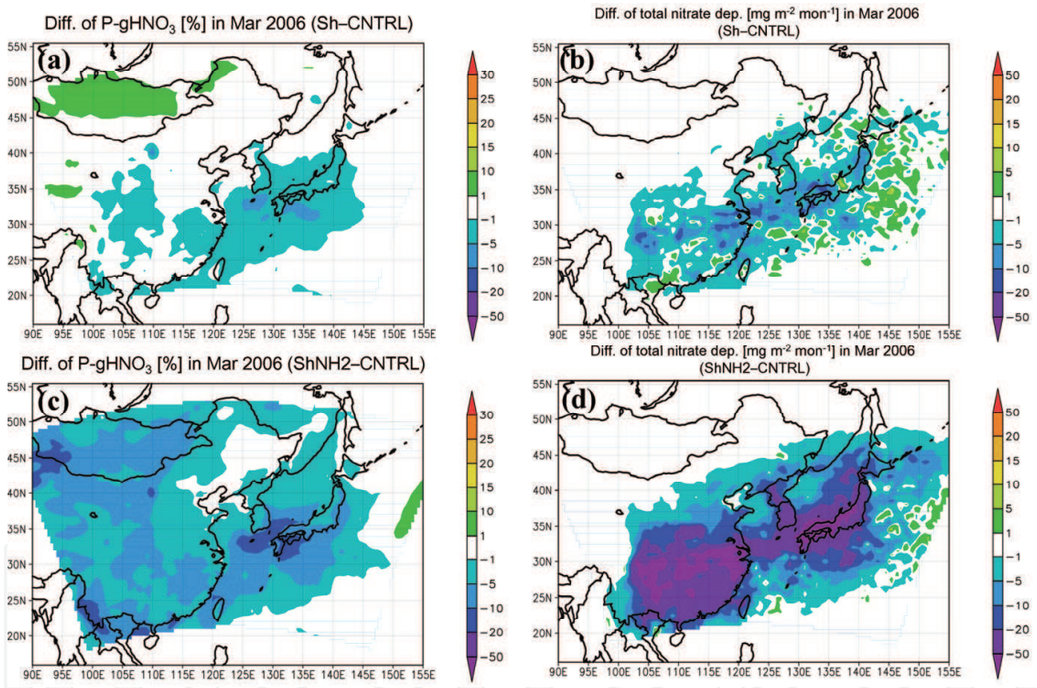

Fig. 11. Spatial distributions of the differences in the gas phase fraction of nitrate (%) (left panels) and total (dry + wet) deposition of nitrate (μg m^{-2} mon^{-1}) (right panels). The upper and lower panels show the results for (Sh – CNTRL) and the (S2NHh – CNTRL) runs, respectively.

As a result of future SO_2 emission decreases, less secondary acidification should occur. However, a decrease in nitrate deposition downwind will also mean that t-NO_3 will be transported longer distances, which may result in increased deposition of t-NO_3 in regions further downwind.

Figure 11 shows changes in the gas phase fraction of nitrate and in total deposition when SO_2 emissions are decreased by half. Both the gas phase fraction of nitrate and total nitrate deposition in downwind regions decrease, by 1–5% and 1–20 mg m^{-2}, respectively (upper

panels). When NH_3, the counterpart of NO_3^- in aerosols, is doubled and SO_2 emissions are halved, the gas phase fraction of nitrate decreases substantially over downwind regions, which results in a significant decrease in total nitrate deposition (20–50 mg m^{-2}). In the Sh run, the surface mean t-NO_3 concentration over Pacific coastal regions of Japan increases by 0.5–2% (not shown) and the increase in the total deposition is about 1–5 mg m^{-2} over the same regions (Figure 11b), although the increase is small compared to the total deposition (100–400 mg m^{-2}, Figure 10b).

5. Conclusion

We studied secondary acidification, which is enhanced deposition of NO_3^- caused by an increase in the SO_4^{2-} concentration, using field observation data as well as numerical simulations of a volcanic eruption event and the long-range transport of air pollutants. Because the vapor pressure of H_2SO_4 gas is extremely low, increased SO_4^{2-} expels NO_3^- in the aerosol phase to the gas phase, resulting in an increase in the HNO_3 gas fraction. As wet and dry deposition rates of HNO_3 gas are considered to be more efficient than those of NO_3^- aerosols, the deposition of total nitrate (HNO_3 gas plus NO_3^- aerosols) is consequently enhanced, even though its total concentration remains unchanged.

Secondary acidification was prominent when the Miyakejima Volcano (180 km south of Tokyo) erupted, emitting a huge amount of SO_2 (9 Tg yr^{-1}) into the lower atmosphere (~2000 m ASL). At the Happo Ridge observatory (1850 m ASL, 300 km north of the volcano), the fraction of gaseous HNO_3 increased from 40% before the eruption to 95% after the eruption, and the bimonthly mean NO_3^- concentration in precipitation increased by 2.7 times after the eruption. The numerical simulation using the RAQM2 model predicted that as a result of the volcanic SO_2 emissions, the SO_4^{2-} concentration would double and the gas phase fraction of t-NO_3 would increase from 20–40% to 22–45% per month on average over central Japan, which is downwind of Miyakejima volcano. The increase of dry and wet deposition due to the volcanic emission was about 0.5–3 and 5–10 (mg m^{-2} mon^{-1}), respectively. Wet deposition was decreased in some regions, probably because CCN activation and cloud droplet formation of NO_3^- aerosols is more efficient than dissolution of HNO_3 gas into water droplets.

At the Japanese EANET monitoring station at Oki, we found positive correlations between the following observational parameters:

1. SO_4^{2-} concentration in atmosphere and gas phase fraction of HNO_3
2. The gas phase fraction of HNO_3 and wet deposition rate of total nitrate
3. A long-range transport indicator and the wet deposition rate of total nitrate

These positive correlations indicate that secondary acidification occurs during the long-range transport of air pollutants from the Asian continent to Japan. Secondary acidification is less efficient in the presence of abundant sea-salt particles, because the contained Na^+ reacts with nitrate to form $NaNO_3$, keeping it in the aerosol phase.

We also simulated secondary acidification due to future anthropogenic SO_2 emission changes using the RAQM2 model. If SO_2 emissions double, the gas phase fraction increases 1–6% over southern China and over the ocean, resulting in an increase of about 10% in total nitrate deposition over the region. The Asian atmosphere is generally ammonia-rich, so the expulsion of NO_3^- to the gas phase is not significant. However, if emission of NH_3, as the counterpart of NO_3^-, is decreased by half, along with the doubling of SO_2 emissions, then the expulsion of NO_3^- is significant and total nitrate deposition over the downwind region increases by as much as 50%. Asian SO_2 emissions are likely to decrease in the future because of the installation of flue-gas desulfurization devices and petroleum refineries. As SO_2 emissions decrease, nitrate deposition may also decrease in downwind regions. On the

other hand, the decrease in nitrate deposition in downwind regions means that total nitrate will be transported greater distances to regions further downwind.

Our results also indicate that to simulate the concentrations and depositions of t-NO_3 accurately, accurate estimations of emission inventories of SO_2 and NH_3 and of its precursor NO_x are important.

Simulated dry deposition velocities and wet scavenging rates include substantial errors and uncertainties in most numerical models, because those parameters are quite difficult to evaluate from observational data. Therefore, as simulation techniques become more advanced, we should revisit this issue again to update our knowledge about what really happens in the atmosphere.

6. Acknowledgment

We thank Dr. Hikaru Satsumabayashi of Nagano Environmental Conservation Research Institute, Japan, for providing measurement data from Happo Ridge and for engaging in meaningful analysis and discussions.

7. References

Abdul-Razzak, H. & Ghan, S. J. (2000). A parameterization of aerosol activation: 2. Multiple aerosol types, *J. Geophys. Res.*, 105, pp.6837-6844, doi:10.1029/1999JD901161.

Adams, P. J.; Seinfeld, J. H.; Koch, D.; Mickley, L. & Jacob, D. (2001). General circulation model assessment of direct radiative forcing by the sulfate-nitrate-ammonium-water inorganic aerosol system. *J. Geophys. Res.*, Vol. 106, No. D1, pp. 1097-1111.

Andreas, R. J. & Kasgnoc, A. D. (1998). A time-averaged inventory of subaerial volcanic sulfur emission. *J. Geophys. Res.*, Vol.103, No.D19, pp.25,251-25,261.

Brook, J. R.; Di-Giovanni, F.; Cakmak, S., & Meyers, T. P. (1997). Estimation of dry deposition velocity using inferential models and site-specific meteorology – Uncertainty due to siting of meteorological towers. *Atmos. Environ.*, Vol. 31, No. 23, pp. 3911-3919

Clarke, L.; Edmonds, J.; Jacoby, H.; Pitcher, H.; Reilly, J. & Richels, R. (2007). Scenarios of greenhouse gas emissions and atmospheric concentrations. Sub-report 2.1A of Synthesis and Assessment Product 2.1 by the U.S. Climate Change Science Program and the Subcommittee on Global Change Research. Department of Energy, Office of Biological & Environmental Research, Washington, 7 DC., USA, 154 pp.

Deushi, M. & Shibata, K. (2011). Development of an MRI Chemistry-Climate Model ver.2 for the study of tropospheric and stratospheric chemistry, *Papers in Meteor. Geophys.*, in press.

Fujino, J.; Matsui, S.; Matsuoka, Y. & Kainuma, M. (2002). AIM/Trend: Policy Interface, Climate Policy Assessment, Eds. M. Kainuma, Y. Matsuoka and T. Morita, Springer, pp.217-232.

Fujino, J.; Nair, R.; Kainuma, M.; Masui, T. & Matsuoka, Y. (2006). Multi-gas mitigation analysis on stabilization scenarios using AIM global model. Multigas Mitigation and Climate Policy. *The Energy Journal Special Issue*.

Hayami, H.; Sakurai, T.; Han, Z.; Ueda, H.; Carmichael, G.; Streets, D.; Holloway, T.; Wang, Z.; Thongboonchoo, N.; Engardt, M.; Bennet, C.; Fung, C.; Chang, A.; Park, S. U.; Kajino, M.; Sartelet, K.; Matsuda, K. & Amann, M. (2008). MICS-Asia II: Model intercomparison and evaluation of particulate sulfate, nitrate and ammonium. *Atmos. Environ.*, Vol.42, pp.3510-3527.

Hijioka, Y.; Matsuoka, Y.; Nishimoto, H.; Masui, M. & Kainuma, M. (2008). Global GHG emissions scenarios under GHG concentration stabilization targets. *J. Global Environ. Eng.*, Vol.13, pp.97-108.

Intergovernmental Panel on Climate Change (2000), *Special Report on Emissions Scenarios,* edited by N. Nakicenovic, 599 pp., Cambridge Univ. Press., New York.

Jylhä, K. (1999a). Relationship between the scavenging coefficient for pollutants in precipitation and the radar reflectivity factor. Part I: derivation. *J. Appl. Meteorol.*, Vol. 38, pp. 1421-1434

Jylhä, K. (1999b). Relationship between the scavenging coefficient for pollutants in precipitation and the radar reflectivity factor. Part II: Applications. *J. Appl. Meteorol.*, Vol. 38, pp. 1435-1447.

Kajino, M. (2011). MADMS : Modal Aerosol Dynamics model for multiple Modes and fractal Shapes in the free-molecular and near-continuum regimes. *J. Aerosol Sci.*, Vol. 42, No. 4, pp.224-248.

Kajino, M . & Kondo, Y. (2011). EMTACS : Development and regional-scale simulation of a size, chemical, mixing type, and soot shape resolved atmospheric particle model. *J. Geophys. Res.*, Vol. 116, D02303, doi :10.1029/2010JD015030

Kajino, M. & Ueda, H. (2007). Increase in nitrate deposition as a result of sulfur dioxide emission increase in Asia: indirect acidification. *Air Pollution Modeling and its Application XVIII.*, Eds. C. Borrego, E. Renner, Elsevier, ISBN:978-0-444-52987-9, pp. 134-143

Kajino, M.; Ueda, H. ; Satsumabayashi, H ; & An, J. (2004). Impacts of the eruption of Miyakejima Volcano on air quality over far east Asia. *J. Geophys. Res.*, Vol. 109, D21204, doi:10.1029/2004JD004762

Kajino, M.; Ueda, H. ; Satsumabayashi, H ; & Han, Z. (2005). Increase in nitrate and chloride deposition in east Asia due to increased sulfate associated with the eruption of Miyakejima Volcano. *J. Geophys. Res.,* Vol. 110, D18203, doi:10.1029/2005JD005879

Kajino, M ; Ueda, H. & Nakayama, S. (2008). Secondary acidification : Changes in gas-aerosol partitioning of semivolatile nitric acid and enhancement of its deposition due to increased emission and concentration of SOx. *J. Geophys. Res.*, Vol.113, D03302, doi:1029/2007JD008635

Kajino, M.; Ueda, H.; Sato, K. & Sakurai, T. (2010). Spatial distribution of the source-receptor relationship of sulfur in Northeast Asia. *Atmos. Chem. Phys. Discuss.*, Vol.10, pp.30,089-30,127.

Kazahaya, K. (2001). Amount of volcanic gases erupted by Miyakejima Volcano, in *Miyakejima Island Eruption and Wide Area Air Pollution* (in Japanese), Jpn. Soc. For Atmos. Environ., pp. 17-26.

Kim, Y. P.; Seinfeld, J. H. & Saxena, P. (1993). Atmospheric gas-aerosol equilibrium: I. Thermodynamic model, *Aerosol Sci. Technol.,* Vol.19, pp.157-181.

Klimont, Z.; Cofala, J.; Schopp, W.; Amann, M.; Streets, D. G.; Ichikawa, Y. & Fujita, S. (2001). Projections of SO_2, NO_x, NH_3 and VOC emissions in East Asia up to 2030, *Water Air Soil Pollut.*, Vol. 130, pp.193-198.

Kurokawa, J.; Ohara, T.; Uno, I.; Hayasaka, M. & Tanimoto, H. (2009). Influence of meteorological variability on interannual variations of springtime boundary layer ozone over Japan during 1981-2005. *Atmos. Chem. Phys.*, Vol. 9, pp.6287-6304.

Lee, S.; Ghim, Y. S.; Kim, Y. P. & Kim, J. Y. (2006). Estimation of the seasonal variation of particulate nitrate and sensitivity to the emission changes in the greater Seoul area. *Atmos. Environ.*, Vol. 40, pp. 3724-3736.

Meng, Z.; Seinfeld, J. H.; Saxena, P.; Kim, Y. P. (1995). Atmospheric gas-aerosol equilibrium: IV. Thermodynamics of carbonates, *Aerosol Sci. Technol.*, Vol.22, pp.131-154

Morino, Y.; Kondo, Y.; Takegawa, N.; Miyaazaki, Y.; Kita, K.; Komazaki, Y.; Fukuda, M.; Miyakawa, T.; Moteki, N. & Worsnop, D. R. (2006). Partitioning of HNO3 and particulate nitrate over Tokyo: Effects of vertical mixing. *J. Geophys. Res.*, Vol. 111, D15215, doi:10.1029/2005JD006887

Moya, M.; Ansari, A. S. & Pandis, S. N. (2001). Partitioning of nitrate and ammonium between the gas and particulate phases during the 1997 IMADA-AVER study in Mexico City. *Atmos. Environ.*, Vol. 35, pp. 1791-1804.

Nemitz, E. & Sutton, M. A. (2004). Gas-particle interactions above a Dutch heathland: III. Modeling the influence of the NH_3-HNO_3-NH_4NO_3 equilibrium on size-segregated particle fluxes. *Atmos. Chem. Phys.*, Vol. 4, pp. 1025-1045.

Ohara, T.; Akimoto, H.; Kurokawa, J.; Horii, J.; Yamaji, K.; Yan, X. & Hayasaka, T. (2007). An Asian emission inventory of anthropogenic emission sources for the period 1980-2020. *Atmos. Chem. Phys.* Vol. 7, pp. 4419-4444.

Riahi, K.; Gruebler, A. & Nakicenovic, N. (2007). Scenarios of long-term socio-economic and environmental development under climate stabilization. *Technological Forecasting and Social Change*, Vol. 74, No. 7, pp.887-935.

Satsumabayashi, H.; Kawamura, M.; Katsuno, T.; Futaki, K.; Murano, K.; Carmichael, G. R.; Kajino, M.; Horiguchi, M. & Ueda, H. (2004). Effects of Miyake volcanic effluents on airborne particles and precipitation in central Japan. *J. Geophys. Res.*, Vol. 109, D19202, doi: 1029/2003JD004204

Schaap, M.; van Loon, M.; ten Brink, H. M.; Dentener, F. J. & Builtjes, P. J. H. (2004). Secondary inorganic aerosol simulations for Europe with special attention to nitrate. *Atmos. Chem. Phys.*, Vol. 4, pp. 857-874

Seinfeld, J. H. & Pandis, S. N. (2006). *Atmospheric Chemistry and Physics: From Air Pollution to Climate Change, second edition,* Wiley Interscience, New York.

Skamarock, W. C.; Klemp, J. B.; Dudhia, J.; Gill, D. O.; Barker, D. M.; Duda, M. G.; Huang, X. Y.; Wang, W. & Powers, J. G. (2008). A description of the advanced research WRF version 3, *Tech. Note, NCAR/TN~475+STR*, 125 pp. Natl. Cent. Atmos. Res., Boulder, Colo.

Streets, D. G.; Bond, T. C.; Carmichael, G. R.; Fernandes, S. D.; Fu, Q.; He, D.; Klimont, Z.; Nelson, S. M.; Tsai, N. Y.; Wang, M. Q.; Woo, J.-H. & Yarber, K. F. (2003). An inventory of gaseous and primary aerosol emissions in Asia in the year 2000. *J. Geophys. Res.*, Vol.108, No.D21, 8809, doi:10.1029/2002JD003093.

van Vuuren, D. P.; den Elzen, M. G. J.; Lucas, P. L.; Eickhout, B.; Strengers, B. J.; van Ruijven, B.; Wonink, S.; van Houdt, R. (2007) Stabilizing greenhouse gas concentrations at low levels: an assessment of reduction strategies and costs. *Climate Change*, 81, pp.119-159.

Zhang, Q.; Streets, D. G.; Carmichael, G. R.; He, K. B.; Huo, H.; Kannari, A.; Klimont, Z.; Partk, I. S.; Reddy, S.; Fu, J. S.; Chen, D.; Duan, L.; Lei, Y.; Wang, L. T. & Yao, Z. L. (2009). Asian emissions in 2006 for the NASA INTEX-B mission. *Atmos. Chem. Phys.*, Vol. 9, pp.5131-5153.

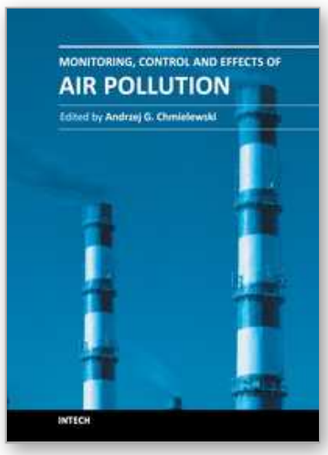

Monitoring, Control and Effects of Air Pollution
Edited by Prof. Andrzej G. Chmielewski

ISBN 978-953-307-526-6
Hard cover, 254 pages
Publisher InTech
Published online 23, August, 2011
Published in print edition August, 2011

The book addresses the subjects related to the selected aspects of pollutants emission, monitoring and their effects. The most of recent publications concentrated on the review of the pollutants emissions from industry, especially power sector. In this one emissions from opencast mining and transport are addressed as well. Beside of SOx and NOx emissions, small particles and other pollutants (e.g. VOC, ammonia) have adverse effect on environment and human being. The natural emissions (e.g. from volcanoes) has contribution to the pollutants concentration and atmospheric chemistry governs speciation of pollutants, as in the case of secondary acidification. The methods of ambient air pollution monitoring based on modern instrumentation allow the verification of dispersion models and balancing of mass emissions. The comfort of everyday humanâ€™s activity is influenced by indoor and public transport vehicles interior air contamination, which is effected even by the professional appliances operation. The outdoor pollution leads to cultural heritage objects deterioration, the mechanism are studied and the methods of rehabilitation developed. However to prevent emissions the new technologies are being developed, the new class of these technologies are plasma processes, which are briefly reviewed at the final part of the book.

How to reference
In order to correctly reference this scholarly work, feel free to copy and paste the following:

Mizuo Kajino and Hiromasa Ueda (2011). Secondary Acidification, Monitoring, Control and Effects of Air Pollution, Prof. Andrzej G. Chmielewski (Ed.), ISBN: 978-953-307-526-6, InTech, Available from: http://www.intechopen.com/books/monitoring-control-and-effects-of-air-pollution/secondary-acidification

INTECH
open science | open minds

InTech Europe
University Campus STeP Ri
Slavka Krautzeka 83/A
51000 Rijeka, Croatia
Phone: +385 (51) 770 447
Fax: +385 (51) 686 166
www.intechopen.com

InTech China
Unit 405, Office Block, Hotel Equatorial Shanghai
No.65, Yan An Road (West), Shanghai, 200040, China
中国上海市延安西路65号上海国际贵都大饭店办公楼405单元
Phone: +86-21-62489820
Fax: +86-21-62489821

IntechOpen